Proceedings of the 21st ICSMGE, Vienna, Austria, 14 – 19 June 2026. Pistrol, Adam & Schweiger (eds.)
Published by: ÖGG, Austrian Society for Geomechanics, Salzburg, Austria, ISBN 978-3-9503898-4-5
https://doi.org/10.53243/ICSMGE2026-424

Membrane-bounded simulations of a sand in a torsional shear test using non-spherical particles.

Javier E. Necochea, **Esteban Sáez**
Departamento de Ingeniería Estructural y Geotécnica, Pontificia Universidad Católica de Chile, Santiago, Chile, esaezr@uc.cl

Javier E. Necochea, Kevin J. Hanley
School of Engineering, Institute of Infrastructure and Environment, The University of Edinburgh, Edinburgh, UK

ABSTRACT: The representation of real-world particles in the Discrete Element Method (DEM) is a common challenge, as many simplifications may be needed to represent quasistatic problems with DEM; however, not all of these are justifiable in dynamic problems. In this study, a poorly graded sand, composed of grains retained between the 1.18 mm and 2.00 mm sieves, was tested in a combined resonant column/torsional shear apparatus at Pontificia Universidad Católica de Chile's Experimental Geotechnics Laboratory. Each tested sample consisted of a cylindrical specimen of height 100 mm and diameter 50 mm, subjected to a confining pressure of 100 kPa, and containing approximately 50,000 grains. This torsional shear test was simulated in DEM, representing grains using different methods: spheres with rolling friction and ellipsoids. Templates for the spherical and ellipsoidal particles were generated from grains scanned using micro-computed tomography. The equivalent-volume spheres and best-fit ellipsoids were extracted from these data. The torsional shear simulations were carried out using the open-source code LIGGGHTS 3.8, using a mix of rigid walls (top and bottom) and a membrane representation using spheres (radial). Grain properties were calibrated with previous direct shear tests. Major differences were seen in the Young's modulus needed to capture the initial shear modulus: 7.5 GPa for spherical particles and 5.0 GPa for ellipsoids. Both spheres and ellipsoids provided a reasonable agreement with laboratory tests at small strains, while at larger strains the shear modulus degradation and the damping were greater in the simulations compared to the real sand sample. These differences in bulk behaviour might be explained by the inability of these simplified shapes to capture the concavity of real particles, underestimating the interlocking between grains. Future research will explore whether a more detailed particle shape representation will enable better agreement with the laboratory data, and the micromechanical differences between the various shape representations.

KEYWORDS: Discrete Element Method, torsional shear, shape effect, ellipsoids, rolling friction.

1 INTRODUCTION

Advances in numerical methods and computational power have made it possible to explore the micromechanical interactions inside granular materials by means of Discrete Element Methods (DEM) modelling (Cundall & Strack, 1979).

DEM has been applied to explore many different geotechnical applications. Most of these simulations have used spherical particles. In reality, soils are not composed of ideal spherical particles; moreover, shape has a considerable influence on soil behaviour (O'Sullivan, 2011). While some methods include indirect shape effects in spheres, such as rolling friction (Ai et al., 2011), micromechanically, there are major differences between spherical and aspherical particles: spheres are not restricted in their rotational degrees of freedom and pack differently from aspherical particles (Necochea et al., 2024).

In this research, we systematically recreate a poorly graded sand using DEM with different grain templates to evaluate the resulting differences in shear modulus degradation and damping, as well their micromechanical properties. In this paper, we compare spheres with added rolling friction and ellipsoids, which are a subset of superquadrics available in LIGGGHTS (Podlozhnyuk et al., 2017), in a torsional shear test.

2 LABORATORY TESTING

The material in this study is a poorly graded sand, composed of grains retained between the 1.18 mm and 2.00 mm sieves.

2.1 *Combined resonant column/torsional shear apparatus*

The sand was tested in the Experimental Geotechnics Laboratory at Pontificia Universidad Católica de Chile using a Controls-WF combined resonant column/torsional shear apparatus at a confinement of 100 kPa. The tested specimen consisted of a cylinder 100 mm tall and 50 mm in diameter, with a total mass of 308.56 grams.

2.2 *Micro-computed tomography scans*

Three samples of the same sand were prepared and imaged using micro-computed tomography at the University of Edinburgh. These three samples, described as small, intermediate, and large, were prepared from further division of the sand with 1.4 mm and 1.7 mm sieves.

Table 1. Average volumes, convexities and sphericities of the different groups of grains from the micro-computed tomography.

Group	Sieve range (mm)	Volume (mm^3)	Convexity	Sphericity
Small	1.18-1.40	1.34	0.84	0.80
Intermediate	1.40-1.70	2.49	0.84	0.80
Large	1.70-2.00	4.23	0.85	0.80

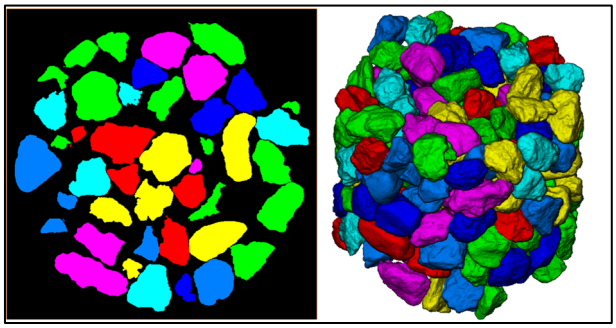

Figure 1. Example of the large sample's reconstructed slices and volumetric image with grain labelling.

The obtained X-ray images were inverted, recreating the volumetric images; then each grain was segmented, obtaining a mesh for each grain as shown in Figure 1. Next, the meshes

were analysed using SHAPE (Angelidakis et al., 2021). Table 1 summarises the nominal size of the sieves used to partition the samples and the average volumes, convexities and sphericities.

Aspect ratios were computed using grains' principal axis lengths from equivalent ellipsoid fits (Angelidakis et al., 2021). The average aspect ratio of the scanned sand was 1.41 between both minor and intermediate principal axis lengths and intermediate and large principal axis lengths.

3 DEM SIMULATIONS

The cyclic torsional shear test was recreated twice using the open-source software LIGGGHTS 3.8 (Kloss et al., 2012): once using spherical particles and once using ellipsoids. The contact model used was Hertz–Mindlin with tangential history. Additionally, an elastic–plastic spring–dashpot (epsd) rolling friction model (Ai et al., 2011) was used for the spherical case. Table 2 presents the grains' properties, which were based on the previous work of Necochea et al. (2024). The Young's modulus was calibrated independently for the spheres and ellipsoids as explained in section 3.4.

Table 2. Grain properties used in the DEM simulations.

Property	Value	Unit
Density	2.65	g/cc
Spheres' Young's modulus	7.50	GN/m^2
Ellipsoids' Young's modulus	5.00	GN/m^2
Interparticle friction coefficient	0.40	-
Particle–wall friction coefficient	0.28	-
Restitution coefficient	0.80	-
Sphere–sphere rolling friction coefficient	0.10	-
Poisson's ratio	0.25	-

3.1 *Grain representation*

To represent the natural variability observed in the tomographic scans of the sample, a total of 40 differently sized templates were used in the simulations. In the spherical case, this is expressed by particles of different radii.

For the ellipsoidal particles, the equivalent volume of the particles is preserved while keeping a fixed aspect ratio of 1.41 between large and intermediate, and intermediate to small, principal axis lengths. Figure 2 presents the spherical and ellipsoidal samples used in the DEM simulations.

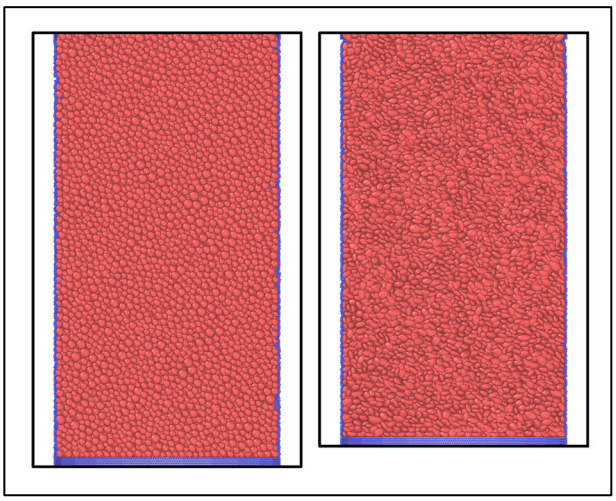

Figure 2. Slice of the spherical (left) and ellipsoidal (right) DEM samples at the confinement stage, viewed from the side.

3.2 *Boundary conditions*

The kinematics of the torsional shear test generates an uneven distribution of the shear stresses at the top of the sample, for this reasons, a periodic boundary approach would not be able to fully capture the interactions to simulate this test, necessitating a more realistic representation of the boundaries. Two implementations of boundary conditions were used for the caps and the membrane.

Firstly, both the top and bottom boundaries were created as triangulated meshes representing laboratory caps. Fins were included in the meshes to improve shear transmission to the sample. Figure 3 shows a close-up of the bottom mesh used in the simulations.

Secondly, the membrane was recreated using a layered distribution of non-bonded spherical particles. The membrane particles' diameter was a constant 0.5 mm, less than a third of the mean grain diameter. These were distributed in layers, each one containing 310 evenly distributed spheres in a circle, to keep particles contained (Wilson & Sáez, 2017; de Bono et al., 2012). The layers were spaced 0.5 mm apart in the vertical direction. Figure 4 presents the initial positions of the particles forming the flexible membrane.

The same Hertz–Mindlin contact model was used between simulated sand grains and the boundaries. The membrane particles were frictionless while two thirds of the interparticle friction was used between the meshes and the sand grains. All interactions between membrane particles were disabled. Table 3 presents the summary of the membrane properties. The Young modulus for the boundaries was the same as for the particles contained in each sample, i.e., in the spherical-particle model the membrane and meshes have a Young's modulus of 7.5 GPa, compared to 5.0 GPa in the ellipsoidal-particle model.

Table 3. Summary of membrane properties used in the DEM simulations.

Property	Value	Unit
Sphere density	1.00	g/cc
Sphere diameter	0.50	mm
Restitution coefficient	0.80	-
Particle–membrane friction coefficient	0.00	-
Poisson's ratio	0.25	-

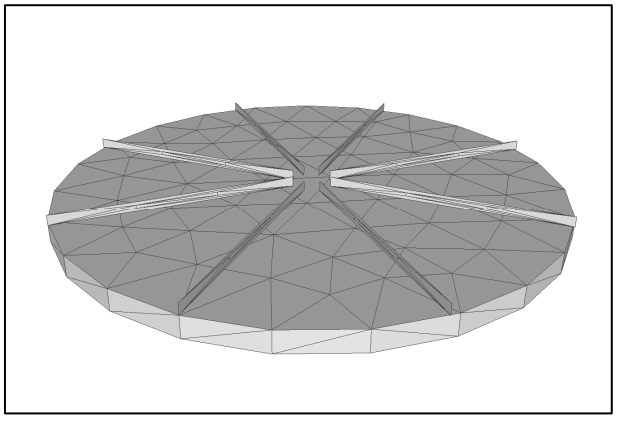

Figure 3. Bottom mesh used to confine the sample. Fins are included to improve shear transfer to the sample.

Finally, to apply the confinement, a servo-controlled vertical stress was imposed on the bottom mesh and, simultaneously, a radial force, in the direction of the cylinder axis, was applied to each membrane particle, similar to de Bono et al. (2012) but without bonding between particles. The particles were only allowed to move in the same radial direction as the applied

force. Figure 5 shows the position of the membrane particles, coloured blue, containing the sand particles, coloured red, at the end of a simulation.

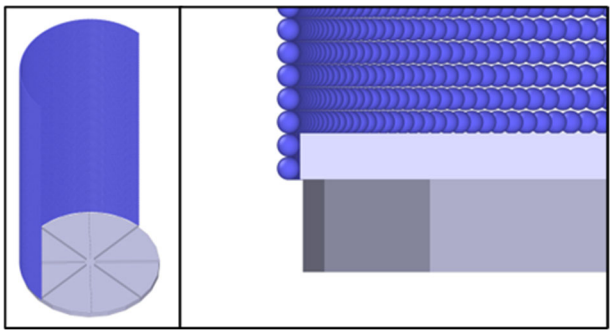

Figure 4. Close-up of the initial distribution of the particles used to simulate the flexible membrane (blue) and the bottom mesh (gray).

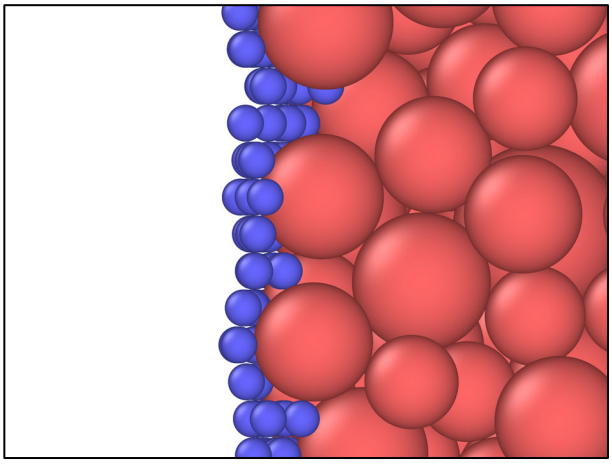

Figure 5. Final position of the membrane particles (blue) containing the material particles (red).

3.3 *Simulation stages*

The simulation has three main stages: particle insertion, confinement and shear. During particle insertion, the top mesh is inactive, the bottom mesh is fixed in place, and the membrane is fixed in its initial position, as seen in Figure 4. Particles are created in a cylindrical volume with double the sample height and then allowed to fall under gravity. Particles are inserted in five layers of 61.71 grams each. A total of 51,576 grains were inserted for both the spherical- and ellipsoidal-particle models.

Once the insertion is completed, the upper mesh is activated and, simultaneously, the servo-controlled stress is initiated in the bottom mesh. Once the meshes have contact with the particles, the radial force acting on the particles is introduced to isotropically confine the sample at 100 kPa.

With the sample confined, the torsional shear begins; a sinusoidal rotation is imposed on the top mesh at a frequency of 1 Hz at five different rotation amplitudes corresponding to shear strains (γ) in a logarithmic space from $5.0\text{x}10^{-4}$% to $5.0\text{x}10^{-2}$%.

3.4 *Calibration*

While most of the particle properties came from the previous study of a direct shear test (Necochea et al., 2024), the calibration process was focused on the stiffness of the particles. In the previous study, the Young's modulus of the particles was below 1 GPa. This proved too soft for the torsional shear test, resulting in a shear modulus below 100 MPa, which is about 30% lower than the experimental value. This highlights the differences between direct shear and torsional shear: while the former aims to describe limit states reaching strains of 20%, the latter seeks to comprehend low-strain behaviour at strains below 0.1%, at least three orders of magnitude lower.

The calibration process aimed to reach a similar initial shear modulus for each of the samples. To achieve this, iterative simulations were conducted, varying the Young's modulus. The final Young's moduli used were 7.5 GPa and 5.0 GPa for the spherical- and ellipsoidal-particle models, respectively.

4 RESULTS AND BULK BEHAVIOUR

The properties of the selected samples at the start of the torsional shear test are presented in Table 4. Both simulated samples were shorter than the real sample's height of 100 mm, particularly the ellipsoidal sample at around 90 mm (visible in Figure 2). This height difference affects the initial void ratio and, accordingly, the initial coordination number of the samples. During the shear testing the heights of the samples change negligibly.

Table 4. Samples' properties at the start of the torsional shear tests.

Sample	Height (mm)	Void ratio	Coordination number
Spherical	95.04	0.602	5.46
Ellipsoidal	90.43	0.525	7.08

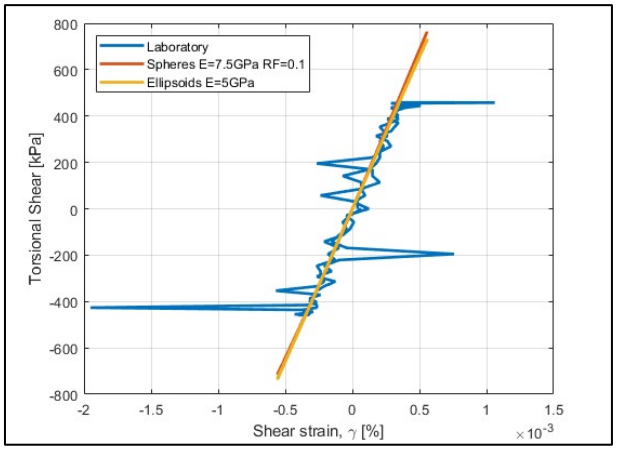

Figure 6. Shear strain vs torsional shear stress evolution at a maximum shear strain of 0.0005% from laboratory data, spherical DEM sample and ellipsoidal DEM sample.

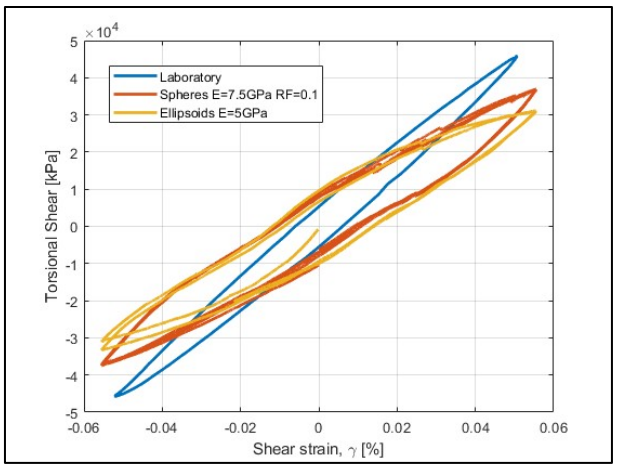

Figure 7. Shear strain vs torsional shear stress evolution at a maximum shear strain of 0.05% from laboratory data, spherical DEM sample and ellipsoidal DEM sample.

From the top mesh, we obtained the torque applied to the sand particles. The shear stress, τ, is calculated by multiplying the torque by $2r/3$, where r is the sample radius, and dividing by

the specimen's polar moment of inertia (Equation (1)). Figure 6 and Figure 7 show the shear stress against the shear strain at the lowest and highest shear strain considered, respectively. The laboratory test presents a narrower loop compared to the simulations with both spheres and ellipsoids.

$$\tau = \frac{2r}{3}\frac{T}{J_p} \quad (1)$$

The degradation of the shear modulus, G, from the laboratory test, and with spherical and ellipsoidal particle shapes in the simulations, is presented in Figure 8. Even though the laboratory and simulation tests start from a similar initial shear modulus of approximately 130 MPa, at larger strains, both simulated curves reach a shear modulus of around 60 MPa compared to 90 MPa for the laboratory test at a shear strain of about 0.065%.

The damping ratio of the simulations is calculated using Equation (2), where A_l is the area of the hysteretic loop, and A_t is the area under the secant modulus line from zero to the peak strain value. Figure 9 presents the damping ratio of the laboratory test and DEM simulations. As expected from the hysteresis loop in Figure 7 the damping at larger strains is overestimated by the simulations; in contrast, at low strains, the simulated samples have close to no damping, implying an almost perfect elastic response.

$$Damping\ ratio = \frac{A_l}{4\,\pi\,A_t} \quad (2)$$

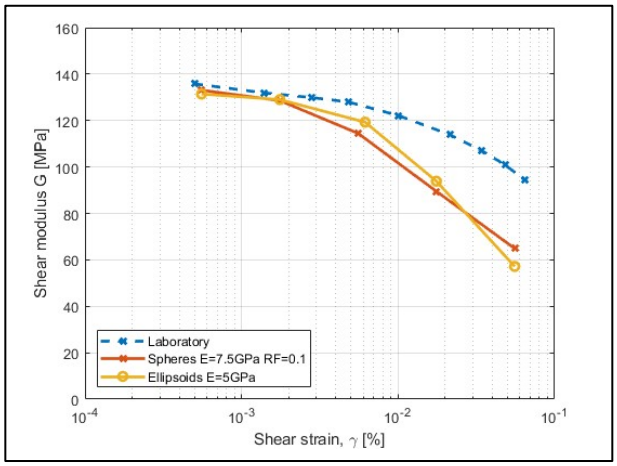

Figure 8. Experimental and DEM stiffness degradation curves.

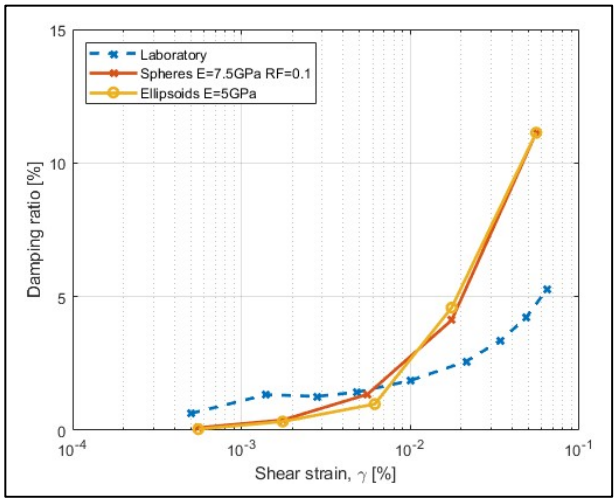

Figure 9. Experimental and DEM damping curves.

5 CONCLUSIONS

While the behaviour at low strains is similar for laboratory and DEM simulations, at larger strains, spheres and ellipsoids present a more pronounced decrease in the shear modulus and a considerable overestimation of the damping ratio. While in some respects purely frictional ellipsoids capture particle shape effects in a similar manner to spheres with rolling friction, these simplified shapes are not well suited to represent real soil particles. Much more intergranular sliding occurs between these shapes than between real sand grains in the equivalent laboratory test. Using these shapes, it is also not possible to capture the initial fabric and void ratio of a real sample.

Spheres and ellipsoids are both fully convex, while the sand particles have natural concavities. As shown in Table 1 the average convexity of the grains is around 0.85. This may induce interlocking between real particles, causing less sliding and, consequently, a more gradual reduction of macroscopic shear modulus and less damping.

Finally, both shape and particle stiffness play a major role in the initial shear modulus: ellipsoids require a lower Young's modulus, 5 GPa, to reach the same initial stiffness as spheres at 7.5 GPa. Interparticle friction and grain shape influence the damping ratio and the shear modulus degradation.

Future work will focus on the micromechanical analysis of these samples and the introduction of multi-spherical clump templates. The latter will augment this shape study with convex particles by enabling interlocking between grains.

6 ACKNOWLEDGEMENTS

The first author acknowledges funding from the Chilean Agencia Nacional de Investigación y Desarrollo (ANID) under the Doctorado Nacional scholarship, number 21200396. This research has also been partially funded by ANID's Fondecyt project number 1250685.

7 REFERENCES

Ai, J., Chen, J.F., Rotter, J.M., and Ooi, J.Y. 2011. Assessment of rolling resistance models in discrete element simulations. *Powder Technology* 206, 269–282.

Angelidakis, V., Nadimi, S., and Utili, S. 2021. SHape Analyser for Particle Engineering (SHAPE): Seamless characterisation and simplification of particle morphology from imaging data. *Computer Physics Communications*, *265*, 107983.

de Bono, J., McDowell, G., and Wanatowski, D. 2012. Discrete element modelling of a flexible membrane for triaxial testing of granular material at high pressures. *Géotechnique Letters*, *2*(4–6), 199–203.

Cundall, P. A., and Strack, O. D. L. 1979. A discrete numerical model for granular assemblies. *Géotechnique*, *29*(1), 47–65.

Kloss, C., Goniva, C., Hager, A., Amberger, S., and Pirker, S. 2012. Models, algorithms and validation for opensource DEM and CFD-DEM. *Progress in Computational Fluid Dynamics*, *12*(2–3), 140–152.

Necochea, J.E., Sáez, E., and Hanley, K.J. 2024. Effect of sand particle shape on micromechanical modeling in direct shear testing. *Computers and Geotechnics* 169(106222).

O'Sullivan, C. (2011). *Particulate Discrete Element Modelling*. CRC Press.

Podlozhnyuk, A., Pirker, S., and Kloss, C. 2017. Efficient implementation of superquadric particles in Discrete Element Method within an open-source framework. *Computational Particle Mechanics*, *4*(1), 101–118.

Wilson, J.F., and Sáez, E. 2017. Use of discrete element modeling to study the stress and strain distribution in cyclic torsional shear tests. *Acta Geotechnica* 12, 511–526.